Dual phases strengthening behavior of Mg−10Gd−1Er−1Zn−0.6Zr alloy

Lin-yue JIA, Wen-bo DU, Zhao-hui WANG, Ke LIU, Shu-bo LI, Zi-jian YU

College of Materials Science and Engineering, Beijing University of Technology, Beijing 100124, China

Abstract: The microstructure evolution and strengthening mechanisms of Mg−10Gd−1Er−1Zn−0.6Zr (wt.%) alloy were focused in the view of the size parameters and volume fraction (f_p) of dual phases (long period stacking ordered (LPSO) structures and β' precipitates). Results show that two types of LPSO phases with different morphologies formed, and the morphology and size of both LPSO phases varied with the solution conditions. However, the volume fraction decreased monotonously with increasing solution temperature, which in turn raised the volume fraction of β' phase during aging. The alloy exhibited an ultimate tensile strength of 352 MPa, a yield strength of 271 MPa, and an elongation of 3.5% after solution treatment at 500 °C for 12 h and aging at 200 °C for 114 h. In contrast to the LPSO phase, the β' phase seems to play a more important role in enhancing the yield strength, and consequently, a decreased $f_{LPSO}/f_{\beta'}$ ratio results in an increased yield strength.

Key words: magnesium alloys; heat treatment; long period stacking ordered (LPSO) structures; precipitate; mechanical properties

1 Introduction

Magnesium (Mg) alloys, as the lightest metallic material for structural applications, have tremendous potential to be used in aerospace and automotive industries [1,2]. In recent years, Mg−Zn−RE (rare earth) alloys (RE/Zn mass ratio >1, RE=Y, Gd, Tb, Dy, Ho, Er, Tm) containing long period stacking ordered (LPSO) structures and/or the solute-segregated stacking faults (SFs) have been attracting considerable attention due to their excellent mechanical performance [3−5]. The mechanical properties are mainly associated with solid solution strengthening and precipitate strengthening. Gd and Er elements have similar atomic radius and high solid solubility in Mg matrix. Especially, Gd addition significantly enhances the age hardening response due to the sharp decline of equilibrium solid solubility of Gd in Mg matrix with decrease in temperature [6,7]. In these Mg alloys, when the content of Gd is above 10 wt.%, Gd is effective in forming dense nanoscale prismatic β' precipitates by peak aging treatment, consequently ensuring that the alloy exhibits strong aging response [8,9]. In addition, the β' prismatic precipitates are generally regarded as the main contributor to the alloy strengthening [7]. Zn addition to Mg−RE alloys remarkably reduces the stacking fault energy (SFE) of basal plane, and gives rise to the formation of LPSO structures and/or SFs, which are beneficial to the improvement of both strength and ductility of Mg−RE alloys [10−12].

Up to now, many LPSO-containing Mg alloys with high mechanical properties have been successfully prepared by conventional thermo-mechanical treatments such as extrusion [13,14],

rolling [15], and ECAP [5]. The previous studies demonstrated the effectiveness of the LPSO structures on strengthening and toughening of Mg alloys. The basal ⟨a⟩ slip and kink bands were considered to be the main deformation modes of LPSO structures during plastic deformation [11]. This is due to the fact that the formation of kink bands relaxed large local strains and led to a relatively homogeneous plastic deformation, the boundaries of which served as obstacles to dislocation motion. Furthermore, the strongly anisotropic deformation behavior of LPSO structures and the strong and stable coherent interface of LPSO/Mg matrix effectively resisted the fracture of Mg alloys [10]. Note that the individual contribution of LPSO structures to the mechanical properties is rarely mentioned in the previous work, probably because it is hard to distinguish the strengthening effect of LPSO structures from various strengthening mechanisms.

Generally, the microstructure, which contains separate LPSO structures or combined LPSO structures with β' precipitates, can be obtained by T4 (solution treatment) or T6 (solution treatment plus artificial aging) heat treatment, respectively. The formation of LPSO structures inevitably consumes the solute elements of RE and Zn in the matrix, and accordingly, the effect of precipitation strengthening during aging process would be reduced. In order to obtain the optimum mechanical properties resulted from the microstructure with co-existing of LPSO structures and precipitates, it is necessary to balance the contents of LPSO structures and precipitates by optimizing the heat treatment conditions. In the present work, we performed various heat treatments on Mg−10Gd− 1Er−1Zn alloy with the aim of investigating the effects of the dual phases (LPSO structures and precipitates) and $f_{LPSO}/f_{\beta'}$ (f: volume fraction) ratio on the mechanical properties. The corresponding strengthening mechanisms were also discussed.

2 Experimental

Mg−10Gd−1Er−1Zn−0.6Zr (wt.%) alloy was melted in electric resistance furnace under a mixture of SF_6/N_2 protective atmosphere. The melt was cast into a steel mold at 730 °C and cooled down in the air. The actual chemical composition of the as-cast alloy was determined to be Mg−10.17Gd−1.35Er−1.20Zn−0.79Zr (wt.%) by using X-ray fluorescence analyzer (XRF, Magic PW2403). Solution treatments (T4 treatments) were carried out at 460, 480, 500 and 520 °C for 12 h, respectively, followed by quenching into water at room temperature. The artificial aging treatment was conducted on the T4-treated samples at 200 °C for 168 h.

Phase analysis was performed by X-ray diffraction (XRD) with Cu K_α radiation. The microstructure was observed with optical microscope (OM) using Zeiss Axio Imager A2m OM, scanning electric microscopy (SEM) using HITACH S3400N SEM equipped with energy dispersive spectrometer (EDS) and transmission electron microscopy (TEM) using JEOL JEM–2100 TEM operating at 200 kV. The average grain size was measured via the linear intercept method, and the volume fraction of phase was determined by an Image-Pro Plus 6.0 software using SEM/TEM images of at least ten different areas for each sample. Thin foil specimen for TEM observation was prepared by mechanical polishing and ion milling using a Gatan precision ion polishing system (GATAN691). The hardness of specimen was measured under a load of 100 g and holding time of 10 s by Vickers hardness testing. Tensile specimens (gauge dimensions: d5 mm × 25 mm) were tested at room temperature under a constant speed of 1.0 mm/min by using DNS–20 universal testing machine.

3 Results

3.1 Microstructures of as-cast and T4-treated alloys

Figures 1(a) and (b) show the OM and SEM images of the as-cast Mg−10Gd−1Er−1Zn−Zr alloy, respectively. It can be seen that the alloy consisted of α-Mg matrix and net-shape primary eutectic phase at grain boundaries. The eutectic phase was identified to have a FCC (face-center-cubic) lattice structure with a parameter of a=0.72 nm by selected area electron diffraction (SAED) from [001], [$\bar{1}$11] and [$\bar{1}$12] directions (Fig. 1(c)). The corresponding EDS result demonstrated that the eutectic phase was $(Mg,Zn)_3Gd$, which is consistent to the previous study [16,17]. In addition, a few fine lamellar phase precipitated in the vicinity of eutectic phase extending into the interior of grains

in unique orientation. The lamellar phases had specific orientation relationship with α-Mg matrix, and they were identified as LPSO structures with a width of several nanometers, in which the grown SFs co-existed (Fig. 1(d)). The average grain size of the as-cast alloy was approximately 28 μm.

The microstructures of as-solution treated alloys at various temperatures are shown in Fig. 2. The volume fraction and morphology of phases varied with the heat treatment temperatures. In comparison with the as-cast alloy, more lamellar-shaped LPSO phase precipitated in the matrix after solution treatment at 460 °C for 12 h. A large number of new block-shaped LPSO phase
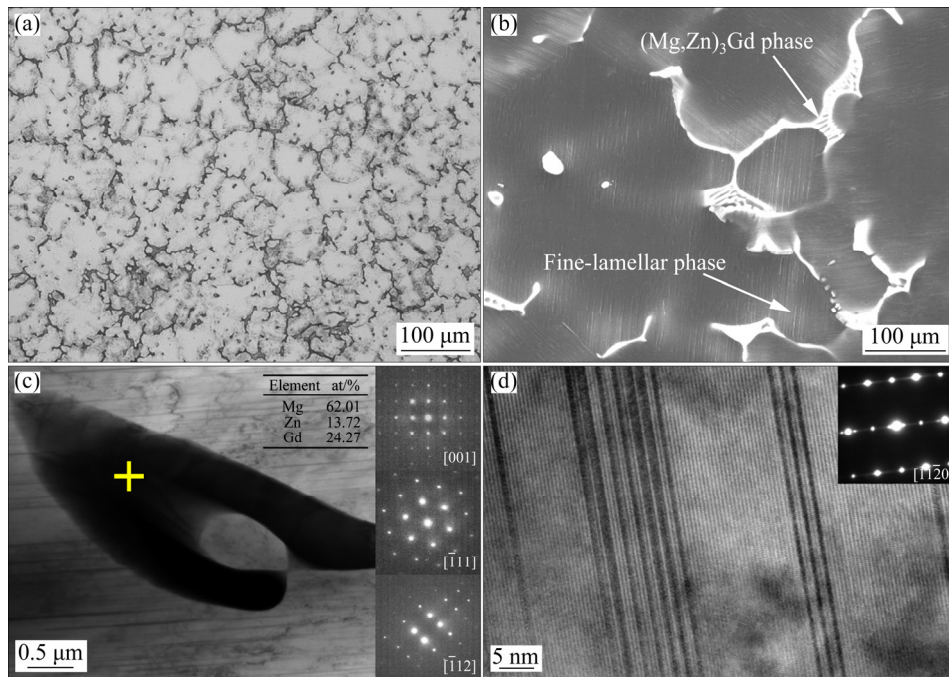

Fig. 1 Microstructures of as-cast alloy: (a) OM image; (b) SEM image; (c) TEM image and EDS result of eutectic phase; (d) TEM image of lamellar phase
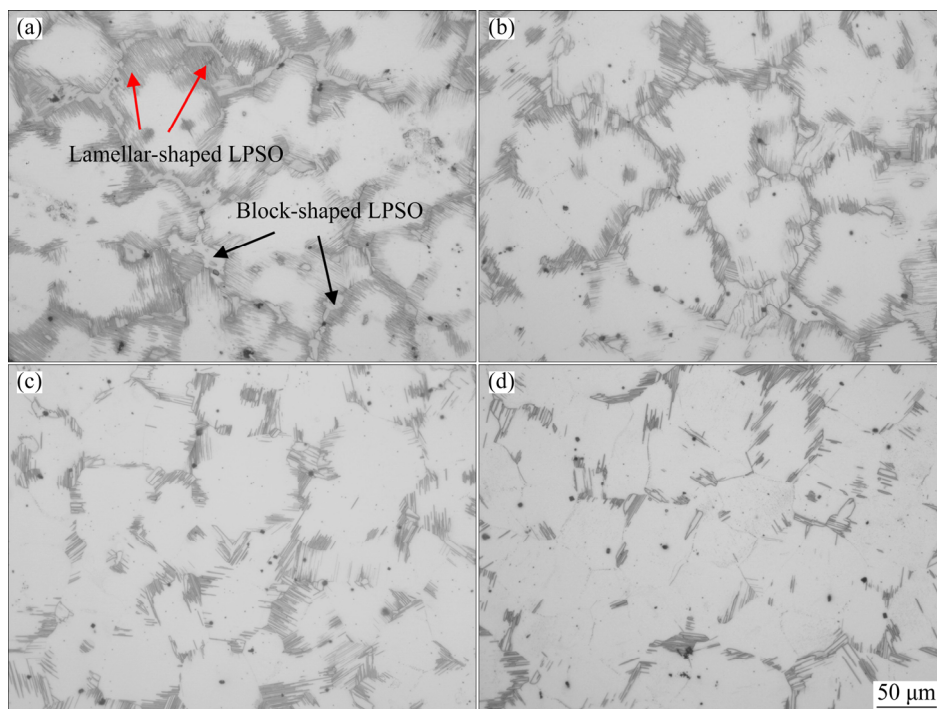

Fig. 2 OM images of as-solution treated alloys at various temperatures: (a) 460 °C; (b) 480 °C; (c) 500 °C; (d) 520 °C

precipitated along grain boundaries, whereas most eutectic (Mg,Zn)$_3$Gd phase dissolved into the matrix (Fig. 2(a)). With the increase in temperature, the amounts of the lamellar-shaped LPSO phase and the block-shaped LPSO phase gradually decreased and (Mg,Zn)$_3$Gd phase was rarely observed (Figs. 2(b−d)). It should be noted that the size (width and length) and morphology of lamellar-shaped LPSO phase in solution-treated samples were different from those in the as-cast ones. The higher temperature led to the higher solution content of Gd, Er and Zn elements in the matrix, and hence, the total amount of LPSO phase was significantly reduced. The average grain sizes of the T4-treated samples grew slightly with the increase in temperature, reaching approximately 31, 33, 36 and 38 μm, respectively.

The volume fractions of (Mg,Zn)$_3$Gd phase and LPSO phase under different conditions are listed in Table 1. In the as-cast alloy, the volume fraction of (Mg,Zn)$_3$Gd phase accounted for 14.8%, while the lamellar-shaped LPSO phase accounted for 3.6%. Following the solution treatment at 460 °C for 12 h, the volume fraction of the block-shaped LPSO phase accounted for 10.5%, and that of the lamellar-shaped LPSO phase increased to 14.2%, whereas that of the (Mg,Zn)$_3$Gd phase decreased to 1.6%. Increasing the solution temperature to 480 °C, the (Mg,Zn)$_3$Gd phase was completely dissolved, and the volume fraction of residual LPSO phase decreased to 8.2% for the block-shaped one and 10.5% for lamellar-shaped one. The solution temperature of 500 °C led to a further reduction of the total volume fraction of LPSO phase to 11.5%. When the solution temperature increased to 520 °C, the total volume fraction reduced to 7.0%, wherein the lamellar-

shaped one accounted for 5.8% and the block-shaped one accounted for the rest.

Figure 3 shows XRD patterns of Mg−10Gd−1Er−1Zn−Zr alloy after various solution treatments. The results indicate that the as-cast alloy mainly consisted of α-Mg matrix and (Mg,Zn)$_3$Gd intermediate phase. After the solution treatments, the (Mg,Zn)$_3$Gd phase almost dissolved into matrix, while the LPSO phase was precipitated from the matrix with the appearance of its characteristic peaks in all T4-treated alloys. In addition, the cuboid-shaped RE-rich phase was only found in the alloy after the solution treatment at 520 °C, which might be due to the high content of solute atoms in α-Mg matrix.
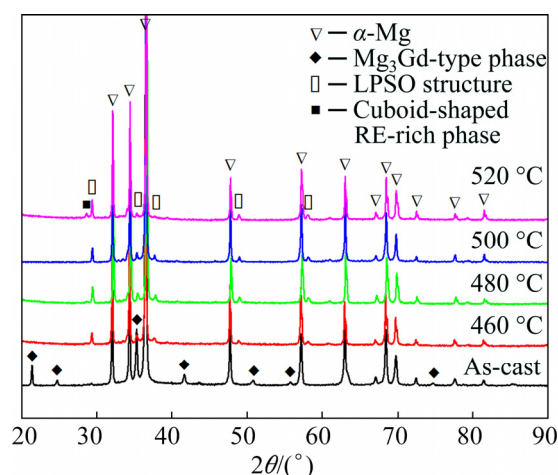

Fig. 3 XRD patterns of as-cast and as-solution treated alloys at various temperatures for 12 h

Figure 4 shows the TEM micrographs of the block-shaped LPSO phase in the alloys T4-treated at various temperatures. Different solution temperature resulted in different sizes of 14H-LPSO phase. The thickness (t) was calculated from the TEM bright field (BF) images along $[11\overline{2}0]_{\alpha\text{-Mg}}$, and the uniform diameter (d_t) was estimated by using corresponding OM and SEM images. The d_t and t of the block-shaped LPSO phase were about 11.2 μm and 1305 nm, respectively, in the alloy after the T4 treatment at 460 °C. As temperature increased, the diameter of the block-shaped and the lamellar-shaped LPSO phase monotonously decreased. The t values of block-shaped LPSO were about 883, 1038 and 442 nm when the alloys were solution-treated at 480, 500 and 520 °C, respectively. The detailed data are listed in Table 2.

Table 1 Volume fractions of (Mg,Zn)$_3$Gd phase and LPSO phase under different conditions

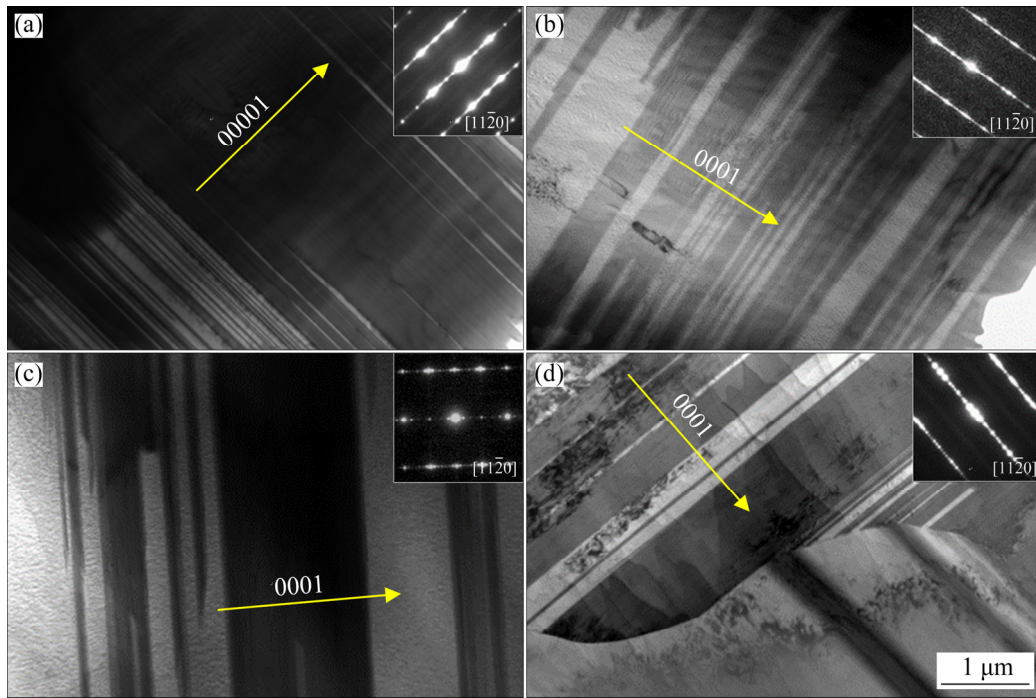| Thermal condition	Volume fraction/%			
	(Mg,Zn)$_3$Gd	Block-shaped LPSO	Lamellar-shaped LPSO	Total
As-cast	14.8	−	3.6	18.4
460 °C, 12 h	1.6	10.5	14.2	26.3
480 °C, 12 h	−	8.2	10.5	18.7
500 °C, 12 h	−	3.6	7.9	11.5
520 °C, 12 h	−	1.2	5.8	7.0

Fig. 4 TEM micrographs along $[11\bar{2}0]_{\alpha\text{-Mg}}$ of block-shaped LPSO phase in as-solution treated alloys at various temperatures for 12 h: (a) 460 °C; (b) 480 °C; (c) 500 °C; (d) 520 °C

Table 2 Relevant data of dual phases under various heat treatment conditions

Thermal condition	Block-shaped LPSO			Lamellar-shaped LPSO			β'			$f_{\text{LPSO}}/f_{\beta'}$
	d_t/μm	t/nm	f_p/%	d_t/μm	t/nm	f_p/%	d_t/nm	t/nm	f_p/%	
(460 °C, 12 h)+ (200 °C, 72 h)	11.2	1305.2	10.5	17.3	24.9	14.2	9.4	8.5	3.8	6.5
(480 °C, 12 h) + (200 °C, 84 h)	7.7	883.4	8.2	12.5	49.3	10.6	11.2	16.3	5.4	3.5
(500 °C, 12 h) + (200 °C, 114 h)	5.7	1038.0	3.6	10.8	61.2	8.0	12.3	25.8	6.6	1.8
(520 °C, 12 h + (200 °C, 78 h)	3.9	442.2	1.2	8.5	29.8	5.8	10.9	31.0	7.4	0.9

β' here means all precipitates forming during aging process, including β'' in alloy solution-treated at 460 °C and β_1 precipitates in alloys solution-treated at 500 and 520 °C

3.2 Age hardening behavior and microstructures of T6-treated alloys

Figure 5 shows the curves of Vickers hardness as a function of aging time of the T6-treated samples. It can be found that the alloy solution-treated at 460, 480 and 500 °C took 72, 84 and 114 h to reach the peak hardness of HV 111, 110 and 112, respectively, whereas the one at 520 °C took 78 h to reach the peak hardness of HV 115 exhibiting the most obvious age-hardening response. Although the increased solution temperature and the consequent raised solid solubility prolonged the arriving of the aging peak, the increase of over-solubility at 520 °C significantly accelerated the solid-solution decomposition during aging, and thus reduces the aging time of peak hardness.
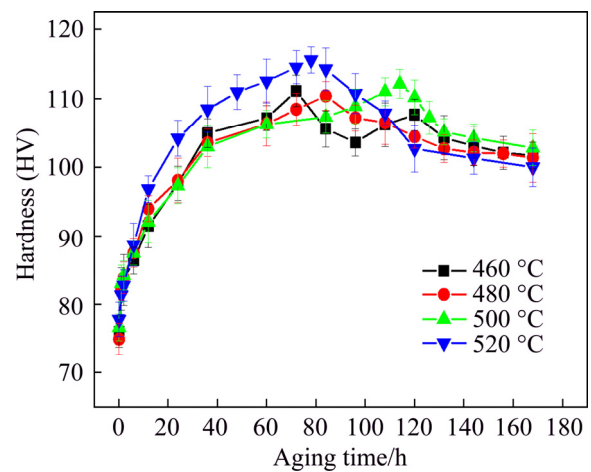

Fig. 5 Age-hardening behavior of alloys at 200 °C after being solution-treated at 460, 480, 500 and 520 °C for 12 h

Besides, the age-hardening response was gradually enhanced with increasing solution temperature.

Figure 6 shows the SEM micrographs of the peak-aged samples. It can be seen that the LPSO phase did not have any change in the morphology during aging treatment compared with that in the T4-treated samples (Fig. 2). No obvious grain growth occurred, indicating that the microstructure of the T4-treated alloys was thermally stable at 200 °C. Since the 14H-LPSO phase maintained superior thermal stability even during hot deformation process [18], the block-shaped and lamellar-shaped LPSO phases could effectively pin grain boundaries and restrict grain growth, enhancing the thermal stability of microstructure. Figure 7 shows the precipitates in the peak-aged samples. In Figs. 7(a) and (b), nearly spherical precipitates (marked by yellow arrowheads) less than 15 nm formed in matrix, and the precipitates were identified as β'' in the peak-aged sample with solution temperature of 460 °C. The BF images and corresponding SAED patterns of the precipitates taken along $[0001]_{\alpha\text{-Mg}}$ (Figs. 7(a, c, e, g)) indicated that the dense nanoscale β' precipitates with base-centered orthorhombic (bco) structure (a=0.650 nm, b=2.272 nm, c=0.521 nm) [7,19] formed in the other T6-treated alloys. Note that the rhombic-shaped β_1 precipitates (marked by red arrowheads) distributing in the vicinity of the β' precipitates also existed in the T6-treated samples with solution temperature of 500 and 520 °C. The lamellar-shaped 14H-typed LPSO phase and SFs were observed on the basal planes of α-Mg matrix in the peak-aged alloys, as shown in Figs. 7(b, d, f, h). The LPSO phase and the β' precipitates formed with an intercalated structure, in which the β' precipitates lay between the LPSO phase. With the thermal stability of the LPSO phase, the spatial interaction hindered the coarsening of both β' precipitates and LPSO phase during the aging treatment, which contributed to the strengthening effect. Table 2 lists the size parameters (d_t and t), volume fraction (f_p) and volume fraction ratio ($f_{\text{LPSO}}/f_{\beta'}$) of the dual phases (LPSO phase and β' precipitates) in the T6-treated alloys under various heat treatment conditions.
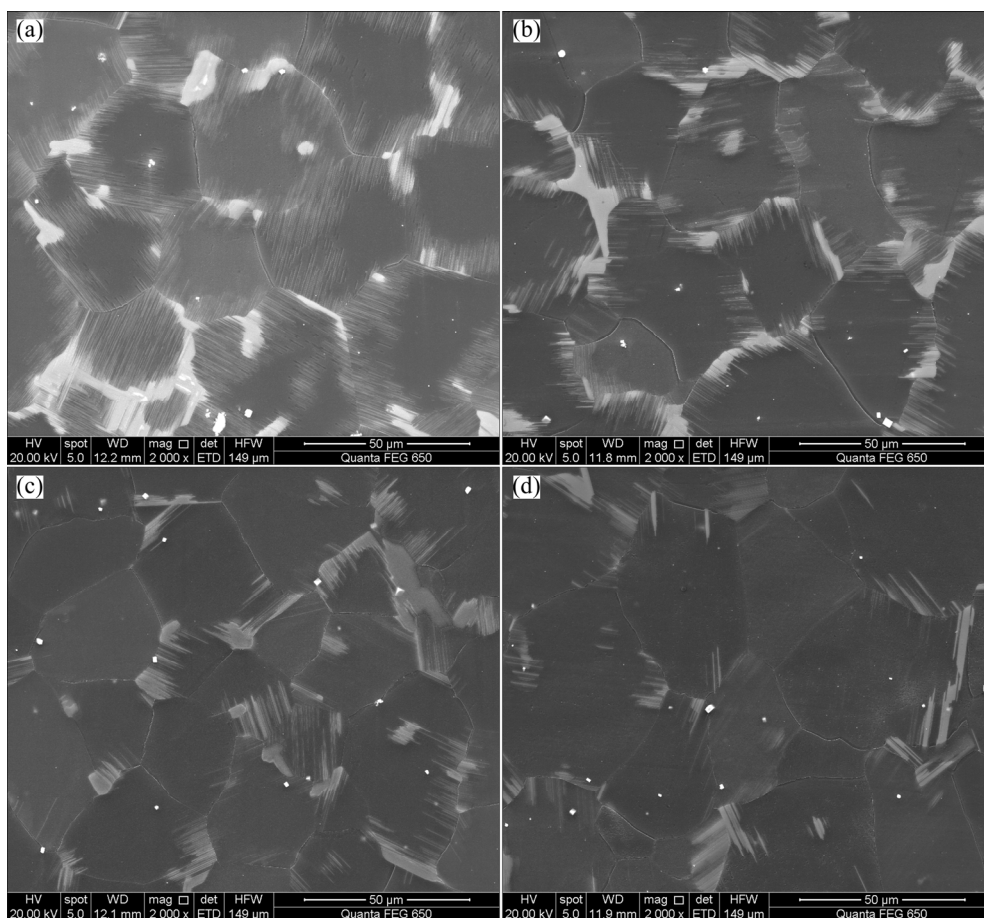

Fig. 6 SEM images of peak-aged samples: (a) (460 °C, 12 h) + (200 °C, 72 h); (b) (480 °C, 12 h) + (200 °C, 84 h); (c) (500 °C, 12 h) + (200 °C, 114 h); (d) (520 °C, 12 h) + (200 °C, 78 h)
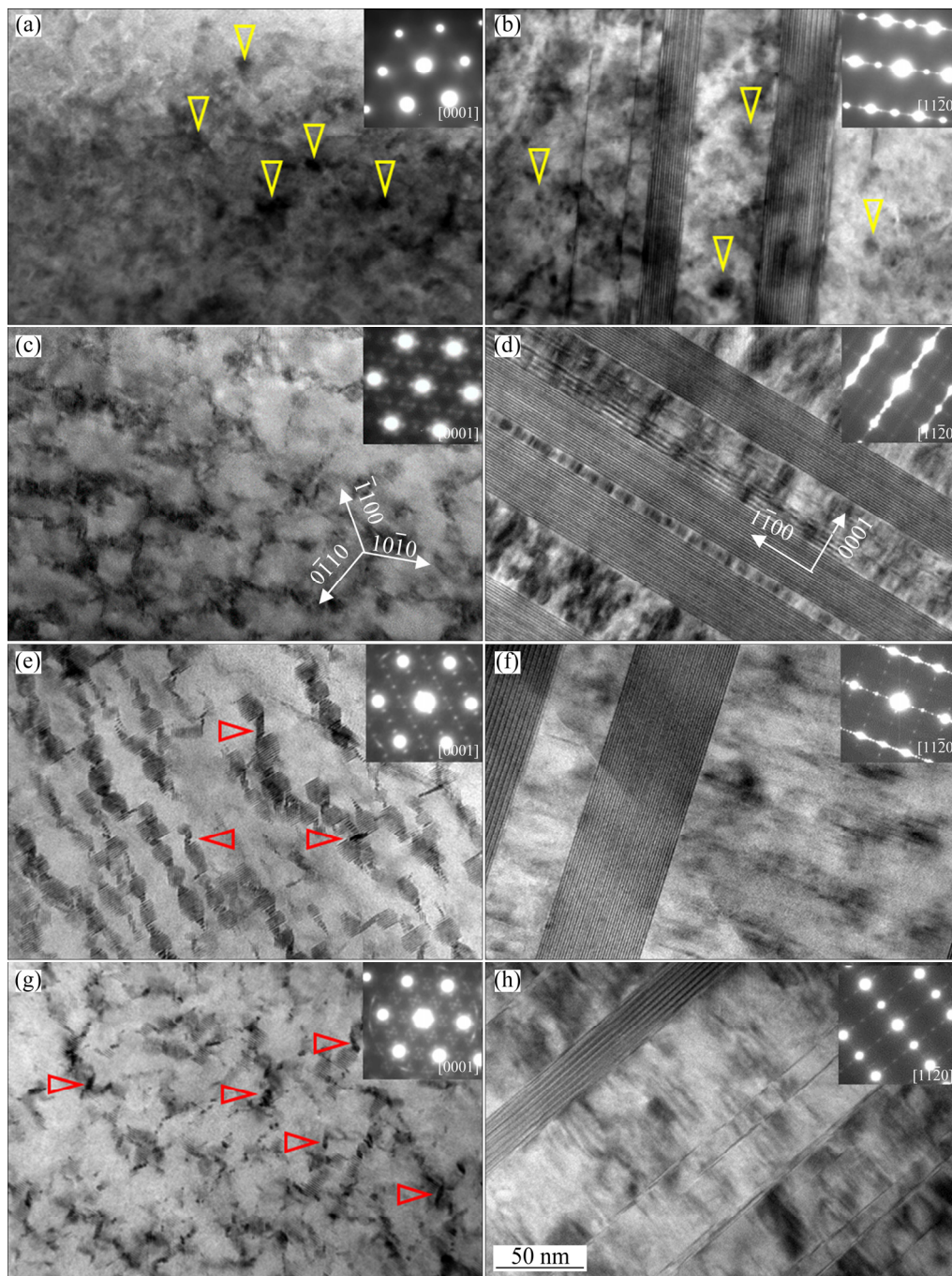
Fig. 7 TEM micrographs of T6-treated alloys at peak-aging state: (a, b) (460 °C, 12 h) + (200 °C, 72 h); (c, d) (480 °C, 12 h) + (200 °C, 84 h); (e, f) (500 °C, 12 h) + (200 °C, 114 h); (g, h) (520 °C, 12 h) + (200 °C, 78 h); (a, c, e, g) BF images taken along $[0001]_{\alpha\text{-Mg}}$ direction; (b, d, f, h) BF images taken along $[11\bar{2}0]_{\alpha\text{-Mg}}$ direction

3.3 Mechanical properties

The variations in tensile properties of Mg−10Gd−1Er−1Zn−0.6Zr (wt.%) alloy at room temperature are summarized in Fig. 8. The detailed data are listed in Table 3. It can be found that the higher solution temperature led to superior mechanical performance, and consequently, the alloy solution-treated at 520 °C exhibited an ultimate tensile strength (UTS) of 271 MPa, a yield strength (YS) of 170 MPa and an elongation of 12.8%. The strength of the T4-treated alloy could be further improved by the following aging treatment, whereas the ductility was deteriorated. The alloy with T6 treatment of (500 °C, 12 h) + (200 °C, 114 h) exhibited an UTS of 352 MPa, a YS of 271 MPa, and an elongation of 3.5%, which turned out to be the best balance of strength and ductility of this alloy.
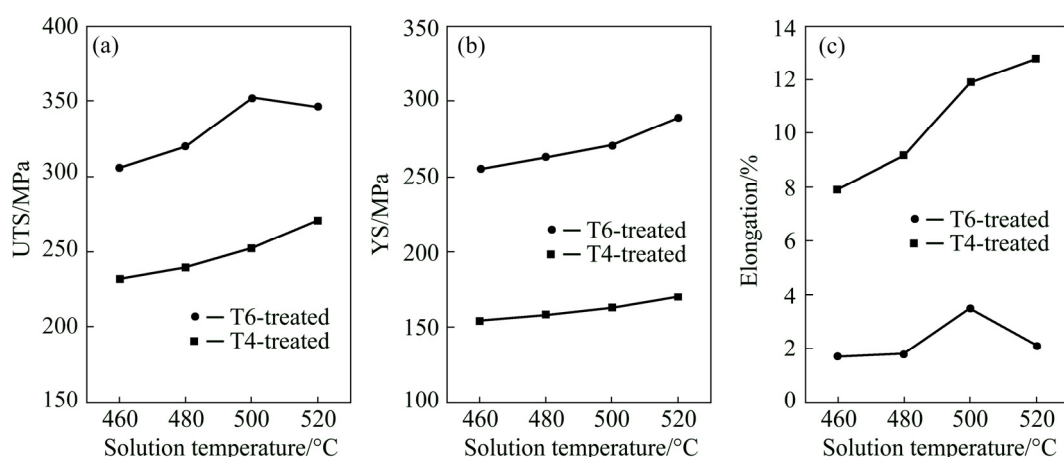
Fig. 8 Mechanical properties of T4- and T6-treated alloys: (a) UTS; (b) YS; (c) Elongation

Table 3 Tensile properties of as-cast, T4-treated and T6-treated alloys at room temperature

Thermal condition		UTS/ MPa	YS/ MPa	Elongation/ %
	As-cast	235	156	10.2
T4-treated	460 °C, 12 h	232	155	7.9
	480 °C, 12 h	240	159	9.2
	500 °C, 12 h	253	163	11.9
	520 °C, 12 h	271	170	12.8
T6-treated	(460 °C, 12 h) + (200 °C, 72 h)	306	255	1.7
	(480 °C, 12 h) + (200 °C, 84 h)	320	263	1.8
	(500 °C, 12 h + (200 °C, 114 h)	352	271	3.5
	(520 °C, 12 h) + (200 °C, 78 h)	346	289	2.1

4 Discussion

Common strengthening mechanisms of magnesium alloys are solid solution strengthening, refinement strengthening, strain strengthening and precipitation strengthening, etc. In the present work, the Mg–10Gd–1Er–1Zn–0.6Zr alloy exhibited different microstructures with respective to the size parameters (d_t and t) and volume fraction (f_p) of LPSO phase and precipitated phase by adjusting the heat treatment conditions. The various phases behaved differently in the alloy strengthening.

4.1 T4 treatment

Usually, the morphologies of LPSO phase present two types in Mg−Gd−Zn based alloys [20]

due to their different formation modes during the solution treatment. The block-shaped LPSO phase is transformed from the primary phase, and the lamellar-shaped one is precipitated from α-Mg matrix. The block-shaped and lamellar-shaped 14H-LPSO phases were observed in the T4-treated samples, and the size and volume fraction of them varied differently depending on the solution conditions. Higher solution temperature accelerated the decomposition of the (Mg,Zn)$_3$Gd phase, and hence, the volume fraction of the block-shaped LPSO phase transforming from the primary phase decreased. The block-shaped LPSO structures mainly distributed along the grain boundaries and had clear edge with α-Mg matrix. It would induce the crack initiation and propagation and deteriorate the ductility of the alloy because of the poor deformation compatibility between the adjacent grains and the block-shaped LPSO structures [21]. Besides, the fine lamellar-shaped LPSO phase composed of very thin LPSO plates and/or grown SFs precipitated during solution treatment. When the solution temperature increased from 460 to 520 °C, the total volume fraction of the block-shaped and lamellar-shaped LPSO phases decreased from 24.7% to 7.0%, which resulted in the continuous increase of elongation of T4-treated alloy from 7.9% to 12.8% (Tables 1 and 3). Note that only ~15 MPa of YS increment was obtained by increasing the solution temperature.

The unit cell *ABCA* of 14H-LPSO structures with heavier Gd/Er and/or Zn atoms segregated in *B* and *C* layers consumed solid solutes in the matrix [10]. Although the alloy can be strengthened by the LPSO phase via short-fiber reinforcement

mechanism, its solution strengthening effect might be reduced because of the decreased solution content. The comprehensive effects of the above mentioned strengthening mechanisms determine whether the strength of the alloy increases or not after different heat treatments. Compared with the as-cast sample and solution-treated samples at higher temperatures, the sample solution-treated at 460 °C had the highest volume fraction of LPSO phase but the lowest strength. As the solution temperature increased, the volume fraction of LPSO phase decreased but the strength of alloy increased. This implies that the strengthening effect of LPSO phase is lower than the solution strengthening effect. Therefore, higher solution temperature should be selected for the Mg−Gd(−Er)−Zn alloy to get higher strength.

4.2 T6 treatment

Precipitation strengthening is one of the most effective methods to improve the mechanical properties of Mg alloys, and the main strengthening phase is β' precipitates on the habit plane of $\{1\bar{1}00\}_{\alpha}$ for Mg−Gd based alloys [22]. The strengthening effect of co-existing basal LPSO/SFs structures and the prismatic β' precipitates in Mg−Gd(−Er)−Zn alloy is higher than that of the single prismatic β' precipitates in Mg−Gd(−Er) alloy [22,23]. However, the ductility of Mg alloy is usually deteriorated after aging treatment. Figure 9 shows the TEM observations near grain boundaries in the peak-aged alloys. In Fig. 9(a), many ellipsoid-like precipitates distributed along the triangular grain boundaries. The magnified region marked by yellow dotted box is shown in Fig. 9(b). It can be seen that the size of the ellipsoid-like precipitates was about 90 nm, and there was no precipitate free zones (PFZs) in the peak-aged sample with solution temperature of 460 °C. However, PFZs were observed along the grain
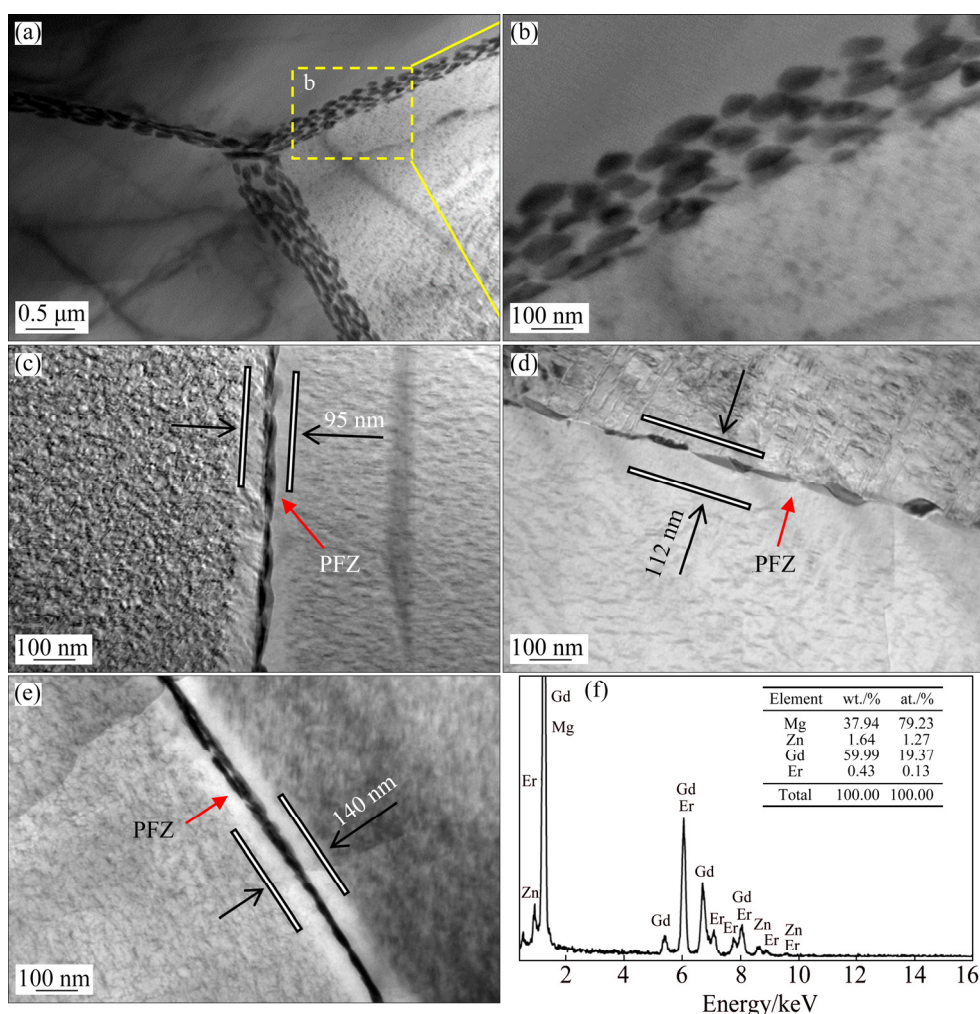

Fig. 9 TEM observations and EDS results near grain boundaries in peak-aged alloys: (a, b) (460 °C, 12 h) + (200 °C, 72 h); (c) (480 °C, 12 h) + (200 °C, 84 h); (d) (500 °C, 12 h) + (200 °C, 114 h); (e, f) (520 °C, 12 h) + (200 °C, 78 h)

boundaries in the peak-aged samples with other solution temperatures, and the morphology of the grain boundary precipitates (Figs. 9(c, d)) was different from that in Fig. 9(b). The grain boundary precipitates became more continuous and the PFZs became wider (Fig. 9(e)), which facilitated the crack initiation and propagation along the grain boundaries. It can be inferred that the poor ductility of T6-treated samples was partially attributed to the PFZs and the $(Mg,Zn)_5(Gd,Er)$ precipitates along grain boundaries.

In addition, the precipitation strengthening is also influenced by the size and number density of precipitates in the α-Mg matrix [24]. As shown in Table 2, the volume fraction of β' precipitates in the alloy reached up to 7.4% under the heat treatment condition of (520 °C, 12 h) + (200 °C, 78 h). The thickness of β' precipitates increased as the volume fraction of the LPSO structures decreased. The present alloy exhibited an UTS of 352 MPa, a YS of 271 MPa, and an elongation of 3.5% under the heat treatment condition of (500 °C, 12 h) + (200 °C, 114 h). Compared with the typical T6-treated Mg−14Gd−3Y−1.8Zn−0.5Zr (wt.%) alloy, having an UTS of 366 MPa, a YS of 230 MPa and an elongation of 2.8% [25], the present alloy was slightly lower in the UTS but higher both in the YS and elongation. It should be noted that the present alloy contains less than 12 wt.% RE elements, which is much lower than that of Mg−14Gd−3Y−1.8Zn−0.5Zr (wt.%) alloy.

The good performance of the present alloy is ascribed to the strengthening effects of the dual phases of LPSO phase and precipitated phase. The precipitation strengthening induced by the dense β' precipitates ($\Delta\tau_{basal}^{\beta'} + \Delta\tau_{pyramidal}^{\beta'}$) can be calculated as follows [6,26]:

$$\Delta\tau_{basal}^{\beta'} = \frac{Gb}{2\pi\sqrt{1-v}\left(\frac{0.953}{\sqrt{f_p}}-1\right)d_t}\ln\frac{d_t}{b} \qquad (1)$$

$$\Delta\tau_{pyramidal}^{\beta'} = \frac{Gb}{2\pi\sqrt{1-v}\times1.139\sqrt{\frac{d_t^2}{f_p}}-1.196d_t}\ln\frac{1.196d_t}{b} \qquad (2)$$

where G is the shear modulus of α-Mg matrix (about 16.6 GPa [27]), b is the absolute value of Burger vector (0.32 nm for Mg [27]) and v is the Poisson ratio (v=0.32). Based on the parameters given above, $\Delta\tau_{basal}^{\beta'}$ and $\Delta\tau_{pyramidal}^{\beta'}$ are calculated

to be 95−132 MPa and 69−88 MPa, respectively. The calculation reveals that the prismatic precipitates are effective in blocking dislocation slip and the contribution of the β' precipitates accounts for a large proportion of YS of the T6-treated alloys. Obviously, the precipitation strengthening effect during aging is much higher than the solution strengthening effect under T4 conditions. Only about 100 MPa increment in YS was obtained after peak-aging treatment, which is lower than the calculated contribution of the β' precipitates. This might be attributed to the reduced effect of solid solution strengthening. From the comprehensive strengthening results of the dual phases (Table 3), the strengthening effect in the form of LPSO phase is limited under both T4 and T6 conditions. Therefore, compared with LPSO phase, the β' precipitates play a more important role in the improvement of yield strength.

Figure 10 shows the relationship between the $f_{LPSO}/f_{\beta'}$ ratio and the tensile properties of the T6-treated Mg−10Gd−1Er−1Zn−0.6Zr alloy. When the ratio is small, the YS of the alloy is higher due to the dense precipitates. Higher volume fraction of β' precipitates leads to higher YS. However, the corresponding poor ductility is probably attributed to the PFZs and the larger grain boundary $(Mg,Zn)_5(Gd,Er)$ precipitates. When the ratio is large, the LPSO phase shows limited contribution to the yield strength, and the large number of block-shaped LPSO residuals at the grain boundaries deteriorates the ductility. It can be seen that better mechanical properties can be achieved when the $f_{LPSO}/f_{\beta'}$ ratio is within an appropriate range.

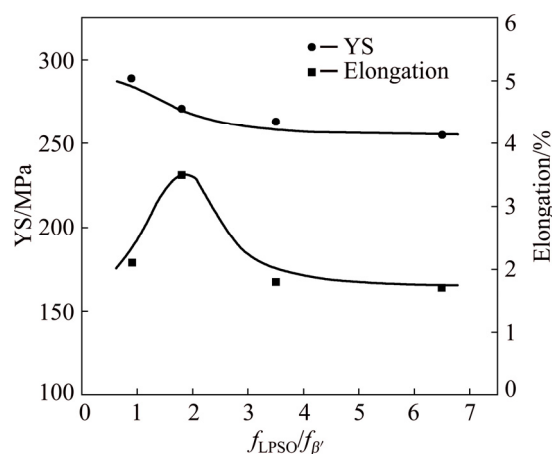**Fig. 10** Relationship between $f_{LPSO}/f_{\beta'}$ ratio and tensile properties of T6-treated alloy

5 Conclusions

(1) The morphology and size of LPSO phase change with the heat treatment conditions, and their volume fraction decreases significantly with increasing solution temperature. Higher solution temperature gives rise to higher solute concentration in the matrix, and consequently, increases the volume fraction of precipitated phase after aging treatment.

(2) The Mg−10Gd−1Er−1Zn−0.6Zr alloy with the heat treatment condition of (500 °C, 12 h) + (200 °C, 114 h) exhibits the best mechanical properties at room temperature: UTS of 352 MPa, YS of 271 MPa, and elongation of 3.5%. The good performance is ascribed to the strengthening of the dual phases, in which the contribution of β' precipitates plays a more important role in alloy strengthening compared with the LPSO phase.

(3) A decreased $f_{LPSO}/f_{\beta'}$ ratio results in an increased yield strength. An appropriate $f_{LPSO}/f_{\beta'}$ ratio is beneficial to obtaining better mechanical properties.

References

[1]   NIE Jian-feng. Physical metallurgy. 20−Physical metallurgy of light alloys [M]. Oxford: Elsevier, 2014: 2009−2156.

[2]   HONO K, NIE J F, OHISHI K. Solute segregation and precipitation in a creep-resistant Mg−Gd−Zn alloy [J]. Acta Materialia, 2008, 56(20): 6061−6076.

[3]   ZHANG Song, YUAN Guang-yin, LU Chen, DING Wen-jiang. The relationship between (Mg,Zn)₃RE phase and 14H-LPSO phase in Mg−Gd−Y−Zn−Zr alloys solidified at different cooling rates [J]. Journal of Alloys and Compounds, 2011, 509(8): 3515−3521.

[4]   RONG Wei, ZHANG Yu, WU Yu-juan, CHEN Yuan-li, TANG Tao, PENG Li-ming, LI Da-yong. Fabrication of high-strength Mg−Gd−Zn−Zr alloys via differential-thermal extrusion [J]. Materials Characterization, 2017, 131: 380−387.

[5]   LU Fu-min, MA Ai-bin, JIANG Jing-hua, CHEN Jing. Enhanced mechanical properties and rolling formability of fine-grained Mg−Gd−Zn−Zr alloy produced by equal-channel angular pressing [J]. Journal of Alloys and Compounds, 2015, 643: 28−33.

[6]   NIE Jian-feng. Effects of precipitate shape and orientation on dispersion strengthening in magnesium alloys [J]. Scripta Materialia, 2003, 48(8): 1009−1015.

[7]   NIE Jian-feng. Precipitation and hardening in magnesium alloys [J]. Metallurgical and Materials Transactions A, 2012, 43(11): 3891−3939.

[8]   YAMADA K, OKUBO Y, SHIONO M. Alloy development

[9]   LI Jun-cai, HE Zong-ling, FU Peng-huai, WU Yu-juan, PENG Li-ming, DING Wen-jiang. Heat treatment and mechanical properties of a high-strength cast Mg−Gd−Zn alloy [J]. Materials Science and Engineering A, 2016, 651: 745−752.

[10]   SHAO Xiao-hong, YANG Zhi-qing, MA Xiu-liang. Strengthening and toughening mechanisms in Mg−Zn−Y alloy with a long period stacking ordered structure [J]. Acta Materialia, 2010, 58(14): 4760−4771.

[11]   KIM J K, SANDLÖBES S, RAABE D. On the room temperature deformation mechanisms of a Mg−Y−Zn alloy with long period stacking ordered structures [J]. Acta Materialia, 2015, 82: 414−423.

[12]   ZHU S M, LAPOVOK R, NIE J F, ESTRIN Y, MATHAUDHU S N. Microstructure and mechanical properties of LPSO phase dominant Mg₈₅.₈Y₇.₁Zn₇.₁ and Mg₈₅.₈Y₇.₁Ni₇.₁ alloys [J]. Materials Science and Engineering A, 2017, 692: 35−42.

[13]   XU C, NAKATA T, QIAO X G. Effect of LPSO and SFs on microstructure evolution and mechanical properties of Mg−Gd−Y−Zn−Zr alloy [J]. Scientific Reports, 2017, 7: 40846.

[14]   YAMASAKI M, ANAN T, YOSHIMOTO S, KAWAMURA Y. Mechanical properties of warm-extruded Mg−Zn−Gd alloy with coherent 14H long periodic stacking ordered structure precipitate [J]. Scripta Materialia, 2005, 53(7): 799−803.

[15]   ZHENG Xiao-bing, DU Wen-bo, WANG Zhao-hui, LI Shu-bo, LIU Ke, DU Xian. Remarkably enhanced mechanical properties of Mg−8Gd−1Er−0.5Zr alloy on the route of extrusion, rolling and aging [J]. Materials Letters, 2018, 212: 155−158.

[16]   WU Yu-juan, ZENG Xiao-qing, LIN Dong-liang, PENG Li-ming, DING Wen-jiang. The microstructure evolution with lamellar 14H-type LPSO structure in an Mg₉₆.₅Gd₂.₅Zn₁ alloy during solid solution heat treatment at 773 K [J]. Journal of Alloys and Compounds, 2009, 477(1): 193−197.

[17]   WU Yu-juan, LIN Dong-liang, ZENG Xiao-qing, PENG Lin-fa, DING Wen-jiang. Formation of a lamellar 14H-type long period stacking ordered structure in an as-cast Mg−Gd−Zn−Zr alloy [J]. Journal of Materials Science, 2009, 44(6): 1607−1612.

[18]   YAMASAKI M, SASAKI M, NISHIJIMA M. Formation of 14H long period stacking ordered structure and profuse stacking faults in Mg−Zn−Gd alloys during isothermal aging at high temperature [J]. Acta Materialia, 2007, 55(20): 6798−6805.

[19]   NISHIJIMA M, HIRAGA K, YAMASAKI M, KAWAMURA Y. Characterization of β' phase precipitates in an Mg−5at%Gd alloy aged in a peak hardness condition, studied by high-angle annular detector dark-field scanning transmission electron microscopy [J]. Materials Transactions, 2006, 47(8): 2109−2112.

[20]   WEN Kai, DU Wen-bo, LIU Ke, WANG Zhao-hui, LI Shu-bo. Precipitation behavior of 14H-LPSO structure in Mg−12Gd−2Er−1Zn−0.6Zr alloy [J]. Rare Metals, 2016, 35(5): 367−373.

[21] XU C Y, FAN G H, NAKATA T, LIANG X, CHI Y Q. Deformation behavior of ultra-strong and ductile Mg−Gd−Y−Zn−Zr alloy with bimodal microstructure [J]. Metallurgical and Materials Transactions A, 2018, 49(5): 1931−1947.

[22] NIE Jian-feng, GAO Xiang, ZHU Su-ming. Enhanced age hardening response and creep resistance of Mg−Gd alloys containing Zn [J]. Scripta Materialia, 2005, 53(9): 1049−1053.

[23] HONMA T, OHKUBO T, KAMADO S, HONO K. Effect of Zn additions on the age-hardening of Mg−2.0Gd−1.2Y−0.2Zr alloys [J]. Acta Materialia, 2007, 55(12): 4137−4150.

[24] ROSALIE J M, SOMEKAWA H, SINGH A, MUKAI T. The effect of size and distribution of rod-shaped β_1' precipitates on the strength and ductility of a Mg−Zn alloy [J]. Materials Science and Engineering A, 2012, 539: 230−237.

[25] ZHANG Song, LIU Wen-cai, GU Xi-yao, LU Chen. Effect of solid solution and aging treatments on the microstructures evolution and mechanical properties of Mg−14Gd−3Y−1.8Zn−0.5Zr alloy [J]. Journal of Alloys and Compounds, 2013, 557: 91−97.

[26] AGNEW S R, MULAY R P, POLESAK F J. In situ neutron diffraction and polycrystal plasticity modeling of a Mg−Y−Nd−Zr alloy: Effects of precipitation on individual deformation mechanisms [J]. Acta Materialia, 2013, 61(10): 3769−3780.

[27] FROST H J, ASHBY M F. Deformation-mechanism maps: the plasticity and creep of metals and ceramics [M]. Pergamon: Oxford, 1982.

Mg−10Gd−1Er−1Zn−0.6Zr 合金的双相强化行为

贾林玥，杜文博，王朝晖，刘 轲，李淑波，于子健

北京工业大学 材料科学与工程学院，北京 100124

摘 要：从长程堆垛有序(LPSO)结构相和 β' 析出相的尺寸参数和体积分数角度，研究 Mg−10Gd−1Er−1Zn−0.6Zr(质量分数，%)合金在不同热处理条件下的组织演变和强化机制。结果表明，经固溶处理后合金中形成两种不同形貌的 LPSO 相，且 LPSO 相的形貌及尺寸随固溶条件发生变化，而其体积分数随固溶温度的升高逐渐减小。LPSO 相体积分数的减小有利于时效过程中 β' 析出相的增加。经(500 ℃，12 h) + (200 ℃，114 h)处理后，合金的室温抗拉强度、屈服强度和伸长率分别达 352 MPa、271 MPa 和 3.5%。β' 相较 LPSO 相更利于合金屈服强度的提高，因此，f_{LPSO}/f_β 值降低，屈服强度提高。

关键词：镁合金；热处理；长程堆垛有序(LPSO)结构；析出相；力学性能

(Edited by Bing YANG)